Full Length Article

Understanding indium nitride thin film growth under ALD conditions by atomic scale modelling: From the bulk to the In-rich layer

Giane B. Damas [*], Karl Rönnby, Henrik Pedersen, Lars Ojamäe [*]

Department of Physics, Chemistry and Biology, Linköping University, 581 83 Linköping, Sweden

ABSTRACT

In recent decades, indium nitride (InN) has been attracting a great deal of attention for its potential applicability in the field of light-emitting diodes (LEDs) and high-frequency electronics. However, the contribution from adsorption- and reaction- related processes at the atomic scale level to the InN growth has not yet been unveiled, limiting the process optimization that is essential to achieve highly crystalline and pure thin films. In this report, we investigate the reaction pathways that are involved in the crystal growth of InN thin film in atomic layer deposition (ALD) techniques from trimethylindium (TMI) and ammonia (NH_3) precursors. To accomplish this task, we use a solid-state approach to perform the *ab-initio* calculations within the Perdew–Burke–Ernzerhof functional (PBE) level of theory. The results clarify the activation role from the N-rich layer to decrease the barrier for the first TMI precursor dissociation from $\Delta^{\ddagger}H = +227$ kJ/mol, in gas phase, to solely $+16$ kJ/mol, in the surface environment. In either case, the subsequent CH_3 release is found to be thermo- and kinetically favored with methylindium (MI) formed at the *hcp* site and ethane (C_2H_6) as the byproduct. In the following step, the TMI physisorption at a nearby occupied *hcp* site promotes the sequential hydrogen removal from the N-rich layer at the minimum energy cost of $\Delta^{\ddagger}H < +105$ kJ/mol with methane (CH_4) release. An alternative mechanism involving the production of CH_4 is also feasible upon dissociation in gas phase. Furthermore, the high concentration of CH_3 radicals, from precursor dissociation, might be the origin of the carbon impurities in this material under the experimental conditions of interest. Finally, the passivation methodology is not found to affect the evaluation of the surface-related processes, whereas the inclusion of spin-polarization is demonstrated to be essential to the proper understanding of the reaction mechanism.

1. Introduction

Light Emitting Diodes (LEDs) constitute a class of dispositives with large applicability in display lighting in electronic devices [1], such as mobile phones and computer screens, as well as in public lighting [1–3], horticulture [4] and medicine [1,5]. The basic principle of LEDs is the assembly of p- and n-doped semiconductors with holes and electrons acting as majority carriers, respectively [1,3,6]. In close contact, the partial overlapping conduction band of these materials enables the diffusion of free electrons towards the p-doped semiconductor, which concentrate near the contact and promotes accumulation of holes in the n-doped part to form the depletion region [4]. This region imposes a barrier to charge transport that is overcome by application of forward bias, with the charge recombination as the main step leading to light emission [4–6]. Therefore, this technology requires the use of semiconductors with direct band gap to avoid the efficiency loss that is commonly associated with phonon-assisted transitions [6].

The Group-III Nitrides are important materials in the history of LED development [6–9]. In the early nineties, the Nobel laureates Amano [7], Akasaki [10] and Nakamura [8,11] published their contribution to the technical achievement of efficient blue LEDs by producing high-quality crystals of Zn- and Mg-doped gallium nitride (GaN). This material has wurtzite and zinc blend crystalline forms, but the preferential form for optoelectronic applications is wurtzite [9,12,13]. In this sense, this wide-band gap semiconductor ($E_g = 3.4$ eV/wurtzite) [14] can be obtained through thin film deposition on sapphire [15], GaAs [16], SiC [17] and graphene [18] substrates by using a set of well-developed methods for crystal growth [9,15–17,19]. High temperatures are usually (800–1000 °C) employed for further decomposition of the precursor materials in gas phase, typically NH_3 and trimethylgallium as nitrogen (N) and gallium (Ga) precursors [20]. At lower temperatures, the reduced gas phase reactivity of certain molecular precursors requires that the major role leading to GaN thin film deposition is played by the surface reactions [17].

Later on, the production of GaN alloys with different composition (AlGaN, InGaN) was of great importance for achieving high efficient LEDs [21–24], an effect that is associated with the quantum confinement [6,25] and the increased carrier capture rate [26] in heterostructures. The alloying strategy also extends the activity of these materials from the ultraviolet–visible towards the near-infrared region, enabling the band gap to be tuned along with the In content [25,27–30]. These factors combined with the electron transport properties and high saturation

---

* Corresponding author.
E-mail addresses: giane.benvinda.damas@liu.se (G.B. Damas), lars.ojamae@liu.se (L. Ojamäe).

electron velocity, making InN highly interesting for high frequency devices, means that studies of InN is important for several technologies [29].

Earlier efforts demonstrated that the metastability of InN at T = 450–550 °C requires a decreased temperature for the crystal growth, which is not favourable for ammonia reactivity in gas phase [31–33]. To resolve this issue, atomic layer deposition (ALD) methods were used for InN growth using trimethylindium (TMI) and ammonia plasma as In an N precursors, respectively, with improved crystalline properties found at T = 320 °C and p = 0.006 bar [34], although In(III) triazenides are also feasible as In precursors [35]. These techniques are well-known for presenting self-limiting chemistry, in which the precursor addition at different time slots imply that the most relevant processes to the growth should occur at the surface [36,37].

From a theoretical point of view, the N-rich layer formation on InN (0001) surface was previously studied by Walkosz *et al.* [38] under metal–organic chemical vapor deposition (MOCVD) experimental conditions. Their outcomes suggest that the NH_3 decomposition involves three main steps: (i) the N precursor (NH_3) is first adsorbed on the top position; (ii) NH_3 is decomposed into NH_2 radicals and H adatoms on bridging and top positions, respectively, and (iii) NH and N species are formed upon H transfer to NH_2 radicals. In a recent work, Rönnby *et al.* demonstrated that the *top*-site adsorption of NH_2 radicals is in fact preferred at lower temperatures[39]. However, there are few reports [28] that have explored the contribution from the In precursor to the crystal growth of indium nitride.

Herein, we perform a thorough investigation on the different reaction pathways leading to the InN crystal growth from NH_3 and TMI precursors by means of *ab-initio* methodology. Initially, we consider that the NH_3 decomposition in gas phase should undergo a route with formation of NH_2 radicals, which should sit at the *top* position with full surface coverage after the first ALD half-cycle. Thereafter, we analyze the TMI decomposition in gas phase and in the surface environment to yield different low-chain hydrocarbons. The main outcomes indicate that the subsequential decomposition of TMI at the surface is thermodynamically and kinetically favoured, where is also necessary to include reaction steps to remove the surface H atoms from the N-rich layer. Moreover, the small barrier for CH_3 release is expected to lead to high concentration of these radicals that in turn might originate the carbon impurities in this material during the growth. In addition, we demonstrate the importance of using spin-polarization effects to properly describe the reaction mechanism.

2. Computational methods

Modelling thin film growth requires a multiscale approach to account for the multiple phenomena occurring in separated time and space scales. At the atomic level, the adsorption equilibrium and activation barriers for diffusion and reaction-related processes of interest are commonly evaluated by means of *ab-initio* methodology [40]. For this reason, we focus on the adsorption thermodynamics and kinetics involved in the crystal growth of InN thin film using TMI and ammonia (NH_3) as indium (In) and N precursors, respectively, with exposure to each starting material occurring at different time slots under ALD conditions. Here, we consider the TMI decomposition in gas phase and surface environment because this precursor could undergo partial dissociation to form CH_3 radicals under the experimental conditions of interest, which could affect the initial steps in the reaction mechanism [41].

The *ab-initio* calculations were carried out using density functional theory (DFT) methods as implemented in the Vienna Ab initio Simulation Package (VASP) [42]. The Perdew–Burke–Ernzerhof functional (PBE) [43] was used to treat the exchange–correlation functional alongside the inclusion of D3-Grimme corrections to account for dispersion and weak interactions at long distances [44]. The cutoff energy for the plane-wave basis set was modified for different system sizes

to reduce the computational effort while still providing an appropriate description of the ground-state energies. The Brillouin zone was integrated within the set of k-points generated by the Monkhorst-Pack scheme, to which a grid was initially provided in accordance with the system size. More detailed information about the level of theory is presented in the Sections 2.1–2.3.

Effects of spin polarization were evaluated in all steps by setting a reasonable initial magnetization moment (mag) that was tuned along with the ionic relaxation. The latter was performed until the atomic forces reached the convergence criterion of 0.01 eV/Å. All atoms in the bulk system were allowed to undergo full relaxation, whereas for the other models at least 1 bottom bilayer was frozen. In addition, the semi-core In *4d* electrons were used explicitly in all calculations to improve the description of this element.

2.1. Bulk structure

The InN wurtzite form crystallizes in the hexagonal space group P6₃mc (group 186) with a= 3.533 Å, c= 5.693 Å and cell volume= 61.54 Å^3, as reported by Wyckoff in 1963 [45]. This crystallographic data was used as starting point for full optimization of the bulk structure with respect to its lattice parameters and ionic positions. The level of theory was set to 800 eV/9–9–9 k-points for cutoff energy/k-point mesh, following the convergence tests that were performed within the range 400–1050 eV and 3–3–3 to 21–21–21 k-points. An alternative conventional cell was also considered for surface studies using lattice vectors that are disposed at an angle of 90° related to each other.

2.2. Surface layer studies

A slab model with growth along the [0001] crystal orientation was built from the bulk structure in order to study the relevant surface reactions. In this step, asymmetric surfaces were generated by breaking In-N bonds, being the bottom/top layer terminated by N/In atoms. The slab thickness was determined by converging the surface energy γ (J/m^2) within the range of 2–9 bilayers, which is defined as [46]

$$\gamma = \frac{E_{slab} - nE_{bulk}}{2A}, \tag{1}$$

where E_{slab} and E_{bulk} correspond to the total energy for the slab and bulk systems, respectively, A is the surface area and n is the number of bilayers. The initial vacuum size of 10 Å was used to block surface interactions with other supercells, with optimizations carried out within the 775 eV/9-9-1 k-points level of theory.

From this point, the surface was expanded into a (2x1) supercell to accommodate the N-based adsorbate, while the bottom layer was passivated by hydrogen atoms with regular (1.00*e*) or fractional (0.75*e*) nuclear charge. The N-rich topmost layer was built by adding NH_2 groups as the main product from NH_3 decomposition with coverage varying from 0.25 to 1.00 ML. The adsorption energy, *i.e.* the energy released with the favourable adsorbate–surface interaction, was determined through the relation

$$E_{ads} = E_{mol+bare} - E_{mol} - E_{bare}, \tag{2}$$

where the first term corresponds to the total energy of the system *after* adsorption ($E_{mol+bare}$) and E_{mol} and E_{bare} are the total energies from the molecular species (NH_2 group or In precursor) and bare surface *prior* to the adsorption process, respectively.

2.3 Precursor adsorption

At this point, the surface area from the conventional cell was expanded into a 3 × 2 surface supercell to accommodate properly the In precursors without allowing any interactions with its nearest images, also requiring a larger vaccum size (15 Å). The level of theory (425 eV/ Γ-point) was set to reduce the computational effort related to large

supercells, while still maintaining a good accuracy in the description of the system and processes. In this step, the bottom layer was passivated by regular hydrogen atoms (+1.00e) as they provide an even number of electrons to the system that is found to be convenient.

The thermal contributions were computed for selected systems through phonon calculations using the code Phonopy [47]. These corrections were then added to the total energy E_{total} to compose the enthalpy H_i and Gibbs free energy of each species G_i:

$$H_i = E_{total} + E_{ZPE} + U_{vib} + pV \tag{3}$$

and

$$G_i = H_i - TS_{vib}. \tag{4}$$

In Eq. (3), E_{total} comprises electronic (from the self-consistent field step) and ionic interaction energy contributions, whereas the zero-point energy correction is given by E_{ZPE}. Lattice vibrational contributions to the internal energy U_{vib} along with the pressure–volume pV term complete the description of H_i, although variations in the latter term are usually negligible in the model herein considered. In Eq. (4), the vibrational entropic contributions S_{vib} and temperature T are added to compose the full Gibbs free energy G_i.

Furthermore, the minimum energy path (MEP) for most reaction steps was determined by simultaneous optimization of a chain of varying number of images linking the equilibrium states, *i.e,* reactants and products. These calculations were carried out using the climbing-image nudged elastic band (CI-NEB) [48–50] method as implemented in the VASP transition state theory (VTST) code. In this approach, the image with highest energy is released from its springs connected to the chain of states to further reach the transition state (TS) region. As an alternative approach, the H abstraction to form CH_4 involves solely three atoms for the TS search. In this case, the z-coordinate of these atoms was varied consistently between the images and constrained until the TS was reached. In both cases, the TS was confirmed through the frequency analysis.

3. Results and discussion

3.1. Bulk structure

Indium has electronic configuration [Kr] $4d^{10}$ $5s^2$ $5p^1$ in its elementary form, but the outermost electrons from s and p shells are partially transferred to nitrogen to form the In-N bond in each tetrahedron entity. The ionic character of this chemical bond is described through Bader analysis, which establishes that the charge carried by each In/N atom is equal to 11.55e/6.45e. Therefore, the partial charge δ= +1.45e/-1.45e for In/N is also indicative of the small charge transfer

(1.45e) between these atoms. The projected density of states depicts the natural contribution from In $4d$ orbitals to compose the valence band maximum (VBM), although In $5p$ (from 0.0 to −3.5 eV) and In $5s$ (at deeper energies starting from −2.5 until −5.4 eV, which is not shown) exhibit more significant contribution. These orbitals hybridize with the dominant N $2p$ orbitals to form a chemical bond with high covalent character, as shown in Fig. S1 in the Supporting Information. Thus, the In-N chemical bond exhibits an ionic-covalent nature with predominant covalent character similar to that verified for GaN [51].

The wurtzite InN has calculated lattice parameters given by a = 3.560 Å, c = 5.763 Å and γ = 120°, which are in excellent agreement with the reported values (a = 3.533 Å and c = 5.693 Å) [45]. Its crystal structure is illustrated in Fig. 1, where the In-N bond length d_{In-N} is equal to 2.173–2.181 Å and the cell volume is 63.35 Å^3. The alternative conventional cell has calculated a= 3.563 Å, b= 6.171 Å, c= 5.760 Å, α = β = γ = 90° and d_{In-N} = 2.18 Å. Furthermore, the good prediction for the cohesive energy E_{coh}= 7.73 eV (E_{exp}= 7.97 eV [52,53]) indicates the reliability of the PBE method to describe the thermodynamic-related quantities for this material.

The band gap E_g of 0.73 eV was initially estimated from the integrated density of states by taking the difference in energy between the VBM and the conduction band minimum (CBM). These limits were established by considering the band-filling towards the completion of the total number of electrons (t= 36.000), a parameter that should remain constant throughout the forbidden region until the first unoccupied band is reached (t ≥ 36.001). Hence, E_g reproduces well the reported value that was previously obtained using optical absorption measurements with low-free electron concentration (E_g= 0.6–0.7 eV) [54–57]. For matters of comparison, the density of states plot returned values for E_g within the range 0.35–0.68 eV, depending on the threshold that is used for analysis (DOS= 0.005–0.020 states/eV). Liang *et al.* found an underestimation of E_g within the PBE level of theory through the band structure analysis [58]. In this sense, each approach has different reliability to determine the direct or indirect band gap in semiconductors, but the PBE level of theory gives a reasonable description of this property in all cases

3.2. Surface layer

3.2.1. Bare surface

As previously mentioned, the primitive unit cell was cut along the [0001] direction for creation of a slab model where relevant surface reactions to the InN crystal growth could be evaluated. The thickness of the model was determined by converging the surface energy γ within the range (2–9 bilayers), based on the assumption that the absence of surface-surface interactions through the bulk layers should provide a
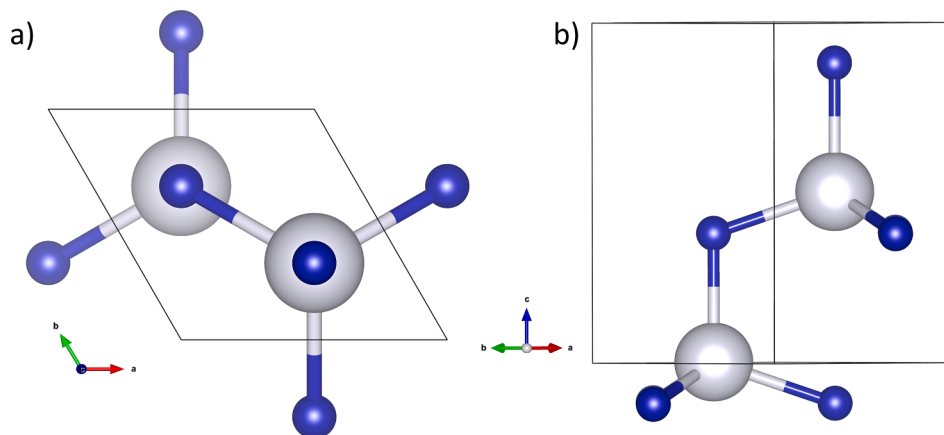
Fig. 1. Bulk crystal structure from wurtzite indium nitride (InN) viewed along the c-axis (a) and laterally (b), as obtained from full relaxation of ionic positions and lattice parameters. Level of theory: 800 eV/9x9x9 k-points.

constant value for the relation given by Eq. (1) [46]. All relevant data regarding γ is available in Table S1 and Figure S2 in the Supporting Information.

The five-bilayer slab presents a well-converged value for γ (1.91 J/m^2), according to our calculations at the 775 eV/9–9-1 k-points level of theory including spin-polarization. Comparatively, Guisbiers et al. [59] have previously estimated γ as 1.42 J/m^2 for this material using similar methodology. The difference of $\sim$ 0.5 J/m^2 related to our study arises mainly from i) the lower k-point mesh used by the authors, and ii) the slight modification in Eq. (1) to replace the total energies by the respective cohesive energies, with the determination of the bulk E_{coh} made through the slope of the slab value and the total number of atoms [59]. However, the lack of experimental reports on γ for InN does not enable us to predict the calculation error for this property in neither study.

(1 × 1) Model. The (1 × 1) five-bilayer surface model has its topmost layer entirely composed by tetrahedral In atoms, whereas unsaturated N atoms terminate the opposite surface. In the latter case, a slight flattening of each InN tetrahedral entity is verified with an In-N-In angle ($a_{\text{In-N-In}}$ = 116.7°) that is higher than regular interlayer values ($a_{\text{In-N-In}}$ = 111.9°). Each surface In atom has total charge of 11.86e (δ= +1.14 e), a value that is ~0.2e higher in comparison with the bulk values (11.57–11.62e). Unsurprisingly, the bottom N atoms (6.20e, δ = 1.20e) exhibit the same trend, with a decrease in ~ 0.2e as result of the dangling bond. At this point, the localization of a small fraction of the electronic charge (0.2e) in the top/bottom layers leads to an overall dipole moment in the system. The inability to localize the charge unity in either surface might also be originating from the inadequacy of the GGA functional to treat such effects [60], instead redistributing it into the bulk layers and altering all partial charges ($\Delta\delta$ < 0.09e/N atom and 0.07e/In) in comparison with the bulk system. Note that we maintain the term *unpaired electron* to denominate the localization of such small fraction of electronic charge over an atom or region in further discussions.

The unpaired electron on each *N* atom at the bottom leads to a slight magnetization in this system (mag= 0.77 μ_b), an effect that is not verified for the top In atom (<0.01 μ_b/atom). Thus, the magnetization is eliminated by saturating the dangling bond with either regular or fractionally charged hydrogen atom (1.00e or 0.75e), as explained in Section 2.2. In either case, it is introduced a net charge of +0.3e/atom in the bottommost layer, although the charge distribution within the N-H bond is slightly different upon charge transfer. In other words, the positive partial charges on the regular and fractionally charged H atoms increase from δ= +0.33 to +0.50e, respectively, as result from the charge transfer to form the N-H bond. As these atoms are not involved in the precursor decomposition, it is safe to affirm that the passivation method will not affect the thermodynamic properties that are discussed in this work. From this point, all models are assumed to be undergone passivation in the bottommost layer with H of nuclear charge equals to 1.00e.

(2 × 1) Model. The lattice vectors from the (1x1) slab model were then shifted by using an appropriate conversion matrix to generate a convenient model with orthogonalized structure (see Fig. 2(a)). Thereafter, the surface area was enlarged into a (2x1) supercell with constrained dimensions a = 7.23 Å, b = 6.26 Å and c = 38.87 Å and $\alpha = \beta = \gamma = 90°$. The presence of unsaturated bonds on the topmost layer leads to a change in atomic hybridization ($sp^3 \rightarrow sp^2$) for half of In atoms and, consequently, to an empty p orbital that is available for further interactions. Fig. 2(b) shows that In surface atoms lying along the *b* axis will alternate stabilization into the trigonal planar (In1) and tetrahedral (In2) geometry in the surface reconstruction. In fact, the (2x1) slab model with reconstructed surface is 0.12 eV (0.03 eV/atom) more stable than the unreconstructed case. Similar findings were reported previously by Walkosz et al. [38] This phenomenon also distorts the tetrahedral geometry of the nearest N atoms, which find competition between the planar- and tetrahedralization to form In-N surface bonds differently angled at 97.79° (In1-N-In3) and 113.03° (In2-N-In3).

This system exhibits small total magnetization (mag= 0.60 μ_B) arising mainly from the tetrahedral In surface atoms (<0.09 μ_B/atom). These atoms should present an unpaired electron as result from the reconstruction (see Fig. 2(b) and Table S2), but their atomic magnetic moments are clearly unaffected by the charge localization. Therefore, the confirmation of the electron unpairing is achieved through Bader analysis, which establishes an excess of negative charge of $\sim$ 0.5e/tetrahedral In atom at the surface, in comparison with the bulk or trigonal planar In atoms. Furthermore, the electron density is redistributed in $\sim$ 0.23e from half of the top surface atoms towards the tetrahedral In atoms, leaving the mentioned empty p orbital in the former case.

On the unreconstructed surface, the tetrahedral In atoms are likely to provide one unpaired electron/atom that leads to an even number of electrons with same band energy. The result is a non-spin polarized solution for the closed shell system that is slightly more favourable (~0.016 eV) in comparison with the spin-polarized case. Here, the magnetization is also 0.60 μ_B, but arises from all four tetrahedral In surface atoms (~0.02 μ_B/atom). The total magnetization and the value obtained per atom are not comparable quantitatively, since only the former is obtained directly from the self-consistent calculations. Additional calculations neglecting the passivation layer reveal mag = 3.30 μ_B, which is much lower than that expected in presence of 4 unpaired electrons on N atoms lying at the bottom layer. In this sense, N atoms exhibit low magnetic moment (~0.40 μ_B/atom), an effect that is likely to be originated from the electron delocalization in the crystal structure, as previously discussed. The use of Hubbard corrections could improve the quantitative description of this property [61], but the final model herein utilized for the evaluation of reaction-related processes does not exhibit magnetization, as discussed in section 3.2.2.
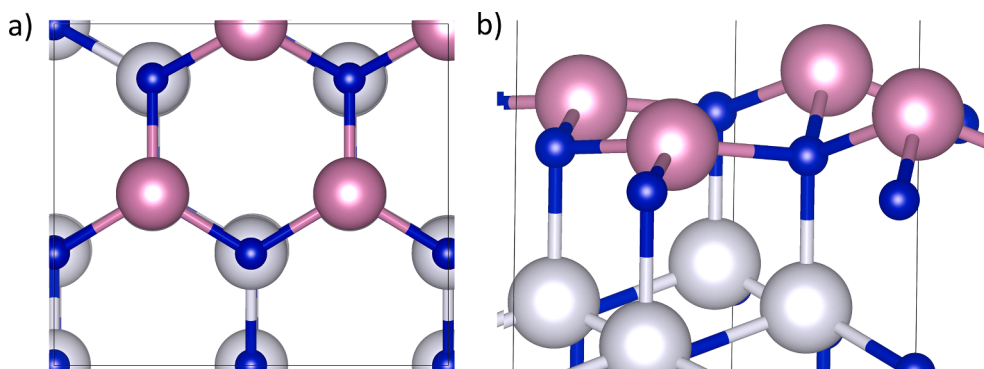
Fig. 2. Bare (2x1) reconstructed surface of InN viewed along the *c* axis (a) and laterally (b). In the latter, the left/right In atoms display sp^2/sp^3 hybridization. Level of theory: 425 eV/3–3-1 k-points. Passivation: H-1.00e, mag = 0.60 μ_B. Color code: silver/light purple (In) and blue (N).

3.2.2. Formation of the N-rich layer

In this subsection, we investigate the formation of the N-rich layer from NH_3 plasma, which was previously used as N precursor for the InN deposition on Si(1 0 0) [34]. The self-limiting chemistry characteristic of ALD techniques [62] imply that the formation of a N-rich layer with full coverage is proceeded before the In precursor is introduced into the deposition chamber [34,63]. At non-equilibrium, the predominant composition should comprise a NH_2-terminated surface with radicals sitting at the *top* site [39]. This pathway does involve H transfer to form NH or N species, as previously proposed for the NH_3 decomposition on InN(0001) surface under MOCVD conditions [38]. In fact, the remaining H atom (from NH_3) should participate in the CH_3 removal (from the In precursor) from the previous half-cycle [34,62].

Fig. 3(a) depicts the bare surface model used for NH_2 adsorption at different coverage states. At low coverage (0.25 ML), NH_2 radicals exhibit preferential adsorption for the bridging (br) site [38], although the on-top adsorption is also feasible with $E_{ads} \sim$ –296 kJ/mol. The latter adsorption type is basically a chemisorption process with the formation of a coordinate covalent bond through the lone pair that is provided by the NH_2 group to a In atom with sp^2 configuration.

Thereafter, the localized charge in the remaining tetrahedral In atoms would be shared with the unpaired electron in the radical to form the covalent bond. As a consequence, the full coverage (1 ML) by NH_2 radicals would imply in the availability of 1–2 electrons for building the In-rich layer.

The central N atom in the free NH_2 radical receives $0.70e$ from both hydrogen atoms to generate a neutral entity with an unpaired electron, which is consistent with mag= 1.00 μ_B. Posterior to the chemical adsorption, the charge transfer towards the central atom reaches $1.23e$ ($|\Delta\delta| = 0.50e$ related to the initial state). As the sp^2 In atoms could only provide $0.1e$ for the In-N bond, the residual charge is likely to be originated from other NH_2 groups with an exposed lone pair. Such charge redistribution leads to an almost negligible localization on each NH_2 group (mag = 0.02 μ_B/atom). It is also valid to mention that the final $\delta= -1.23e$ for each N atom lies in between the value for the free molecule ($\delta_N= -0.70e$) and the bulk atom ($\delta_N=-1.42e$).

From Tables 1 and S3 it is evident the small effect from the passivation method on E_{ads} (<19 kJ/mol) or the inclusion of spin-polarization given in parenthesis (<3 kJ/mol). Moreover, the last column in Table 1 displays the likelihood to form the NH_2-terminated surface (NH_2*) from NH_3 decomposition, which is computed as the formation energy of NH_2* through the equation

$$NH_3(g) + \text{ bare} \rightarrow NH_2* + 1/2H_2(g). \quad (5)$$
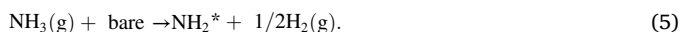
The NH_2* formation energies expressed in Table 1 (−16.0 to −95.2 kJ/mol) indicate that this is a thermodynamic favourable process in all cases. These values are given for completeness, since the surface should be covered by CH_3 groups at the beginning of the NH_3 half-cycle.

Nonetheless, the lateral interactions exerted by adsorbates sitting nearby each other has a larger effect on these properties. For instance, the amount of energy released per adsorbed molecule (E_{ads}/NH_2), in the second column in Table 1, is decreased in 13 % for 1 ML NH_2 ($\sim$ –258 kJ/mol) in comparison with 0.25 or 0.50 ML coverage. Similarly, the formation energy for the full covered surface is 77.2 kJ/mol less negative than the 0.75 ML case. This indicates the presence of repulsive interactions between NH_2 radicals via H···H atoms that are distanced from each other by 2.57–2.63 Å. On the other hand, the N···H attractive interactions at 2.49–2.75 Å help in the stabilization of this layer compared to the absence of such interactions.

3.3. Indium precursor studies

In this section, we explore the different reaction pathways for the In-rich layer formation during the InN crystal growth. The end point should be the MI formation, as the NH_3 plasma is expected to remove the last precursor ligand in the next half-cycle [34,62]. Initially, the investigation is carried out at T= 0 K to include the large number of mechanistic possibilities that are discussed in Sections 3.3.1–3.3.2. Then, the most feasible pathways are selected for the inclusion of thermal effects in Section 3.3.3.

Here, it is important to define the different thermodynamic quantities that are discussed: E and ΔE stand for the total energy (in kJ/mol) of a certain structural configuration referenced to the initial system and to the system *prior* to that step, respectively. Equivalently, H and G correspond to the enthalpy and Gibbs free energy at the temperature of interest referenced to the initial system. The asterisk (*) indicates that the species is adsorbed through physical and/or chemical interactions.

3.3.1. Trimethylindium decomposition to yield ethane

In Gas Phase. The trimethylindium (TMI) precursor is a trigonal planar molecule with internal angles of 120° and bond length $d_{In-C}=$ 2.18 Å. The Pauling electronegativity for these atoms (In: 1.78, C: 2.55) [64] imposesa polarity to the In-C chemical bond with subsequent charge transfer of $\sim$ 1.1e from indium to carbon atoms ($\delta_C=$ –0.46 to −0.49e). In a previous study, Hwang *et* al. used Raman spectroscopy to find that TMI undergoes through thermal decomposition in presence of N_2 carrier, starting at temperature T = 120 °C up to 535 °C [41]. The sequential loss of CH_3 radicals is predicted to be a feasible route for the TMI decomposition in different gas carriers [41,65]. However, it is important to mention that the range of temperature could still be altered with varying experimental conditions [41].

The first CH_3 loss depicted in Fig. 4 (a) and (b) was reproduced by initially placing the TMI molecule in the middle of an empty box with dimensions a= 26.09 Å, b= 21.32 Å, c= 25.53 Å and $\alpha = \gamma = 90.3°$. From
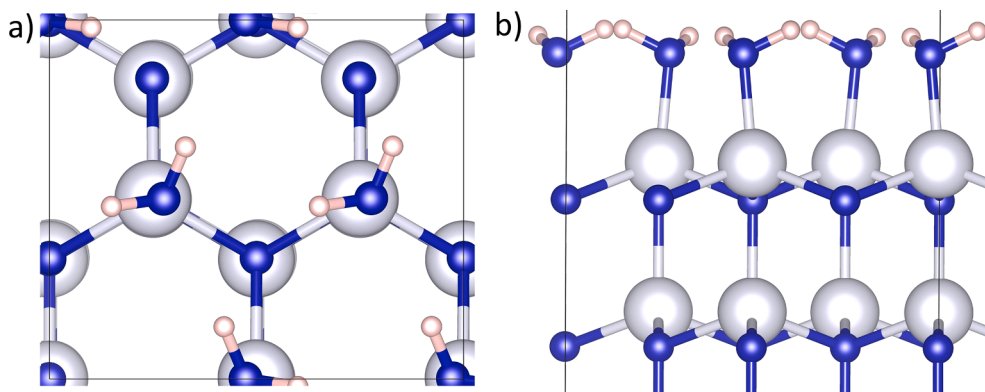
Fig. 3. NH_2 (1ML) adsorption on the reconstructed surface of InN viewed along the c axis (a) and laterally (b). The covalent bond formed with the In surface atoms will lead to either a lone pair or an unpaired electron available on each NH_2 group for the formation of the next layer. Level of theory: 425 eV/3–3-1 k-points. Color code: silver (In), blue (N) and white (H).

Table 1

Adsorption and formation energies (kJ/mol) calculated for NH_2 radicals with different coverages resulting from NH_2 adsorption and NH_3 decomposition, respectively. The values in parenthesis correspond to spin-polarized calculations. Level of theory: 425 eV/3–3-1 k-points. Passivation method: H-1.00e.

Coverage (ML)	Adsorption Energies (kJ/mol)		Formation Energies (kJ/mol)
	Total	/NH_2 group	-
0.25	−296.2(−295.3)	−296.2(−295.3)	−43.7(−42.5)
0.50	−588.6(−585.7)	−294.3(−293.3)	−85.8(−83.8)
0.75	−852.9(−851.0)	−284.6(−283.7)	−95.2(−93.2)
1.00	−1028.5(−1026.6)	−257.6(−256.7)	−18.0(−16.0)

this point, the CH_3 group was moved to a sufficient distance to not feel the electrostatic attraction exerted by the precursor at ~ 4.7 Å. The dissociation product in gas phase, *i.e.* dimethylindium (DMI), has angular geometry with slightly stretched bond length $d_{In\text{-}C}$= 2.22 Å and $a_{C\text{-}In\text{-}C}$ = 120.3° after ionic relaxation. Thus, it is natural that $δ_C$ in the CH_3 radical decreases in ~0.3e ($δ_C$ = −0.2e) due to the dissociation. The energy cost associated with this step is E= +262 kJ/mol within the PBE/ 800 eV/1x1x1 level of theory, which is in fair agreement with other experimental (E_{exp}= +235 kJ/mol) [41] and theoretical reports using the B3LYP method [65]. Including thermal effects leads to $Δ^{‡}H$= +231 kJ/mol at 300 K, therefore representing an agreement of 98% with the aforementioned experimental value [41].

The next step concerns on the DMI adsorption onto the *N*-rich surface at the bridging or hollow site, as the top position is not feasible. At this stage, the InN model was built using a three-bilayer system with (3x2) surface area, with additional change in the level of theory (425 eV/ 1–1–1 k-points) to follow the increase in system size. The data in Table 2 clarifies the preferential adsorption of the DMI precursor onto the *fcc* site by 22 kJ/mol related to the *hcp* configuration. Even though the partial charges for the carbon atoms do not distinguish the In-C bond strength in each case (see Fig. 4(c)), these atoms exhibit mag = 0.2 $μ_B$/atom that promotes a slight planarization of the CH_3 groups (a ~ 113°) at the *fcc* site. Turning on the spin-polarization enhances the precursor stabilization at this position, but culminates in the release of the CH_3 radical from the *hcp* configuration to generate an even more favourable chemisorbed species, MI, with E_{ads}= −563 kJ/mol. Therefore, it is important to keep in mind that a pathway involving this site is also plausible, though involving minor changes in the reaction mechanism.

Further stabilization from the DMI adsorption at the *fcc* site is found through CH_3 loss, an almost barrierless step that releases 187 kJ/mol in relation to the initial species, as shown in Fig. 4(d). The DMI dissociation

in gas phase (E_{diss}= +381 kJ/mol) provides us the importance of such NH_2 groups to weaken the In-C bond and promote the radical release. It is expected that the positive δ= +1.41e exhibited by the In atom in TMI remains unaltered after the CH_3 release, but the smaller change verified for the nearest NH_2 groups ($δ_N$ < 0.05/atom) suggests their inner ability to relocate and redistribute the charge density to other surface NH_2 groups. Therefore, the In-N covalent bonds have their strengthen verified with the significant decrease in 128 kJ/mol in the adsorption energy compared to DMI (see Table 2). From a molecular standpoint, the In-NH_2 bonds have mixed type with main covalent and coordinate covalent character, thus providing an explanation to the instability with the presence of a fifth chemical bond (In-CH_3) before the CH_3 group is released.

The displacement of the MI species towards the *hcp* position is represented in Fig. 4(d) and (e), occurring with an activation barrier $Δ^{‡}E$ of ~ 14 kJ/mol to reach a minimum that is solely 4 kJ/mol higher in energy (E= −183 kJ/mol). Finally, Fig. 4 (f) shows that C_2H_6 is yielded in the highly favourable thermodynamic process given by E = -588 kJ/mol.

On Surface. Assuming that TMI could still be present at the surface during the deposition, another route could be drawn to describe the precursor decomposition to yield C_2H_6, in which the CH_3 radical could be removed or included into the model depicted in Fig. 5 and Figure S3. In either case, MI remains chemisorbed in a *hcp* configuration while covalently bonded to regular NH_2 groups. Furthermore, it is evaluated an alternative pathway that leads to CH_4 formation.

Initially, TMI sits on a stable top-position with adsorption energy equals to −92 kJ/mol (see Fig. 5 (a) and Table 2). This value is similar than that exhibited for the Si precursor on a NH_2-terminated surface for SiN deposition [66], but it is significantly lower in comparison with the NH_2 adsorption for *N*-rich layer formation, with E_{ads}= −296 kJ/mol at 0.25 ML. The much weaker N···In (TMI) interaction leads to a stretching
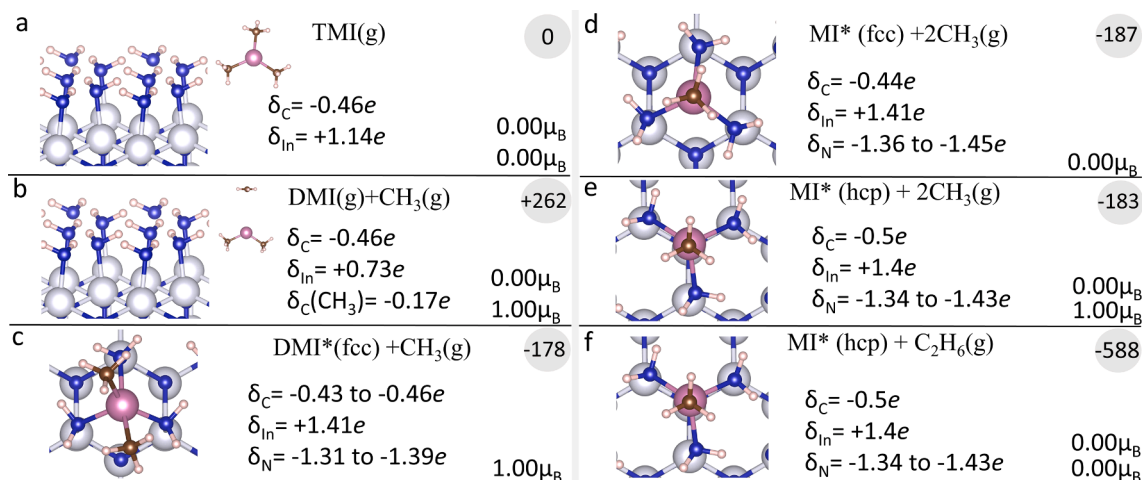
Fig. 4. Reaction pathways for MI and C_2H_6 formation from TMI decomposition in gas phase. The initial TMI* in (a) is decomposed into DMI and CH_3 radical with $Δ^{‡}E$= +262 kJ/mol (b). Further adsorption onto the *N*-rich surface takes place, preferentially, at the *fcc* position (c), followed by the loss of another radical (d-e) to yield C_2H_6 (f). In detail, it is shown the total energies (in kJ/mol, top right), magnetization (in $μ_b$, bottom right), and partial charges (δ) for each system. Note that the asterisk (*) represents an adsorbed species. The gray filled circles at the top right represent minimum points in the potential energy surface. Color code: purple/silver (In precursor/bulk), blue (N), brown (C) and white (H). Level of theory: 425 eV/1–1–1 k-points.

Table 2
Adsorption Energies (kJ/mol) and bond/interaction distances calculated for the NH$_2$ group (0.25 ML) and different In-based precursors. Level of theory: 425 eV/ 3–3-1 k-points (NH$_2$) and 1–1–1 k-points (In-based precursors).

| Adsorbate	Adsorption Energies (kJ/mol)	d_{In-N} (Å)	d_{In-C}(Å) After adsorption	Gas Phase
NH$_2$(top)	−296	2.11	–	–
TMI(top)	−92	2.29	2.20–2.30	2.19
DMI(br)	−406	2.25	2.20	2.22
DMI(hcp)	−418	2.23–2.31	2.30	2.22
DMI(fcc)	−440	2.20–2.24	2.29–2.36	2.22
MI(hcp)	−563	2.17–2.21	2.18	2.26
MI(fcc)	−568	2.18–2.20	2.18	2.26

of such distance by 0.18 Å (d_{In-N}= 2.29 Å, see Table 2), that is caused by the need of accommodating the large CH$_3$ groups in an approximate tetrahedral geometry. In comparison with TMI(g), there is solely an increase by ~ 0.1e in the partial charge from In (+1.20e), while δ_C is altered from −0.46e to a range up to −0.55e as a result of having chemical bonds with different strength. In this sense, the lowest value for δ_C (–0.45e) is shown by the CH$_3$ group sitting closest to the NH$_2$ group, in which the former displays tendency to planarization with a_{H-C-H} ~ 113° and d_{C-H} = 2.30 Å. At this point, the magnetization moment at the carbon atom (0.15 μ$_B$) gives hint about the radical formation in further steps.

It is also noticeable that the homolytic dissociation of TMI at the surface is reduced from E_{diss}= +262 kJ/mol, in gas phase, to solely +22 kJ/mol in the surface environment. In order to understand this activation effect, we performed additional calculations substituting the In-CH$_3$ by In-NH$_2$ bonds in gas phase, with relevant data available in in Table S4. In(NH$_2$)$_3$ displays dissociation energy of +289 kJ/mol, thus being +27 kJ/mol higher than the original TMI. This fact combined with an increased charge transfer from In atom (δ_{In}) and shortened In-N bond on In(NH$_2$)$_3$ evidences the stronger nature of the In-N bond in comparison with In-C. Therefore, it is natural that the energy necessary to break the In-CH$_3$ bonds at the surface are compensated by the favoured

In-N interactions occurring upon physisorption.

The first CH$_3$ elimination leaves DMI adsorbed at the bridging (br) position with release of 75 kJ/mol related to the initial system. This step occurs through the displacement of the initial TMI* to form a transition state (TS) that lies close to the *top* position, at the cost of 21 kJ/mol. The metastable structure displayed in Fig. 5(b) is the final point of the aforementioned displacement, which has an approximate *hcp* configuration (mod-hcp) with even lower energy than the initial adsorbate (ΔE = –34 kJ/mol). In TMI*(mod-hcp), the decreased charge transfer to C atoms (δ < -0.45e) alongside the higher value for In (δ= +1.30e) indicates the weakening of the In-C bonds in favour to the In···N interactions that are formed. This is also verified by two longer In-C bonds (d ~ 2.36 Å) in comparison with the In···N interactions (d ~ 2.26 Å) in this structure. Including the spin-polarization effects allows the CH$_3$ radical elimination that is illustrated in Fig. 5(c), as this species obviously requires the electron unpairing at the carbon atom to be considered. Such radical remains weakly adsorbed at the *hcp* site, with E_{ads} ~ –22 kJ/mol, but is initially eliminated from the model in Fig. 5 (d) to facilitate the analysis.

The further displacement of DMI*(br) towards the *hcp* position upon the activation barrier of 21 kJ/mol leads to the non-magnetized structure displayed in Fig. 5 (e). This adsorbate is covalently bound to 2 NH$_2$ groups with d_{In-N} ~ 2.23 Å, but the decrease in solely 12 kJ/mol for E_{ads} = –418 kJ/mol related to the bridging site suggests that the third interaction with the NH$_2$ group situated at the south position has dipole–dipole nature. Therefore, it is expected that this interaction would exhibit the longest distance (d_{In-N} = 2.31 Å) alongside the In-C covalent bond (d_{In-C} = 2.30 Å, δ = -0.46e). The spin-polarized solution (mag= 1.00 μ$_B$) leads to another minimum in the potential energy surface (PES) in which the CH$_3$ radical leaves the precursor but remains weakly physisorbed through the H$_3$C··· H$_2$N interaction (see Fig. 5(f)). The CH$_3$ release leaves MI sitting at the *hcp* position to form a stable tetrahedral geometry through covalent bonds with the nearest NH$_2$ groups and E_{ads}= –563 kJ/mol. As a consequence, the bond distance between the interacting atoms is shortened to d_{In-N} = 2.17–2.21 Å and d_{In-C}= 2.18 Å, as well as δ_N = -1.37e from the south NH$_2$ group is
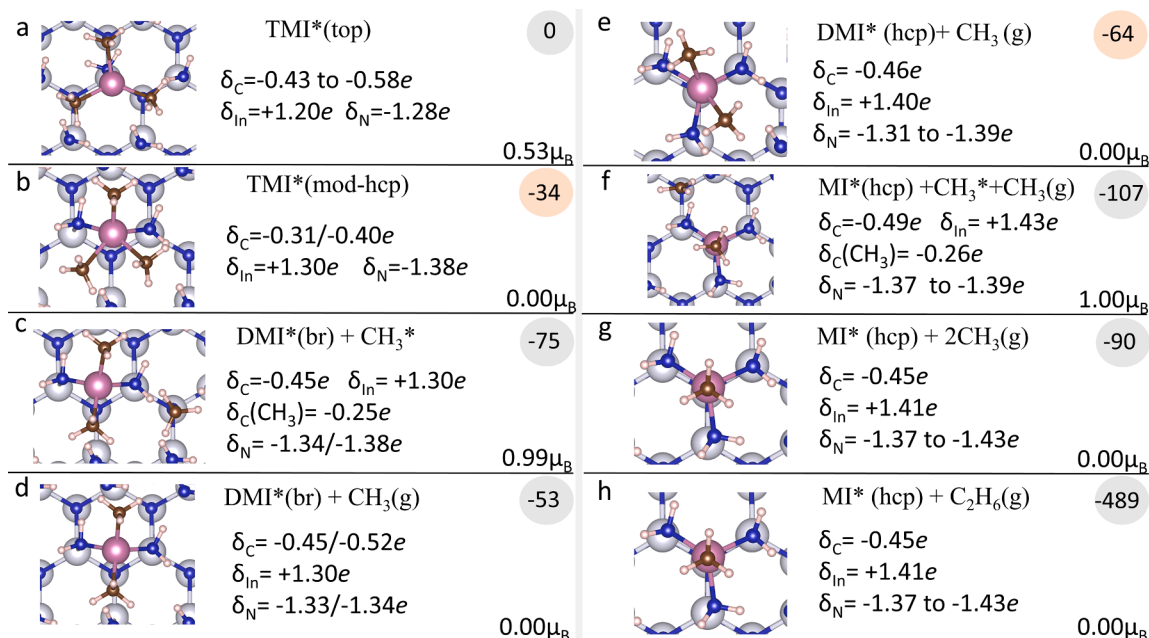
Fig. 5. Reaction pathways for MI and C$_2$H$_6$ formation from TMI decomposition on the surface. The initial TMI* in (a) is displaced towards the modified (mod-hcp) hcp position in (b) with $\Delta^{\ddagger}E$= +21 kJ/mol. Thereafter, it releases subsequentially each CH$_3$ group (c-g) until the final product is obtained in (h). In detail, it is shown the total energies related to TMI* (in kJ/mol, top right), magnetization (in μ$_b$, bottom right), and partial charges (δ) for each system. The silver filled circles represent minimum points in the potential energy surface (PES), whereas the decomposition is imminent after applying spin-polarization effects on the structures represented by the orange filled circles.

diminished due to the stronger In-C and In-N bonds in MI. The CH$_3$* removal from the model in Fig. 5(g) gives E$_{ads}$= –17 kJ/mol for this structure. Finally, the ethane formation in gas phase is a highly favourable process with E= –489 kJ/mol, thus not requiring any activation energy to take place from the previous step. As expected, this value is + 99 kJ/mol lower than the final product obtained through TMI decomposition in gas phase, with E = –588 kJ/mol, since the TMI adsorption enhances the precursor stabilization in ∼ 99 kJ/mol. For matters of comparison, the hydrogen removal at this stage through CH$_4$ formation is much less favourable with the release of solely 92 kJ/mol in the end of the process.

Previous reports have attributed the occurrence of carbon impurities in ALD-driven growth of InN using TMI precursor to the inherently strong In-C bonds, especially in MI [67,68]. In gas phase, our calculations shows that the In-CH$_3$ in MI indeed requires a high amount of energy for further dissociation, with E$_{diss}$ reaching +625 kJ/mol. However, this quantity is significantly reduced to + 179 kJ/mol upon chemisorption onto the hcp site, a fact that indicates the CH$_3$ remotion in the next NH$_3$ pulse is benefited from the adsorption. On the other hand, the CH$_3$ release at each decomposition step is a favourable process that could play a role in the occurrence of such impurities, justifying the inclusion of the CH$_3$ radical in some reaction models.

In Fig. S3, it is illustrated an alternative mechanism that includes the CH$_3$* radical in the model in all steps. In this case, the displacement to the hcp position in Fig. S3(d) is accompanied by the formation of a C-N bond at the adjacent NH$_2$ group, releasing 332 kJ/mol to originate a highly stable structure (E = –407 kJ/mol). The formation of the covalent bond is corroborated by the charge transferred to the nitrogen atom (δ$_C$= +0.20e), clearly showing that such NH$_2$ groups could display different types of chemical bonds with the precursor, as well as dipole–dipole weak interactions with the central atom. In this pathway, the C-N bond should be broken at the cost of ΔE= +322 kJ/mol to form the system shown in Fig. S3 (e). In fact, this bond is even stronger than the In-NH$_2$ bond, with E$_{diss}$= +119 kJ/mol when connected to the CH$_3$ group, suggesting that etching the surface would be more likely to occur than the removal of chemisorbed CH$_3$ groups. These outcomes indicate that the carbon impurities using these precursors might be originating
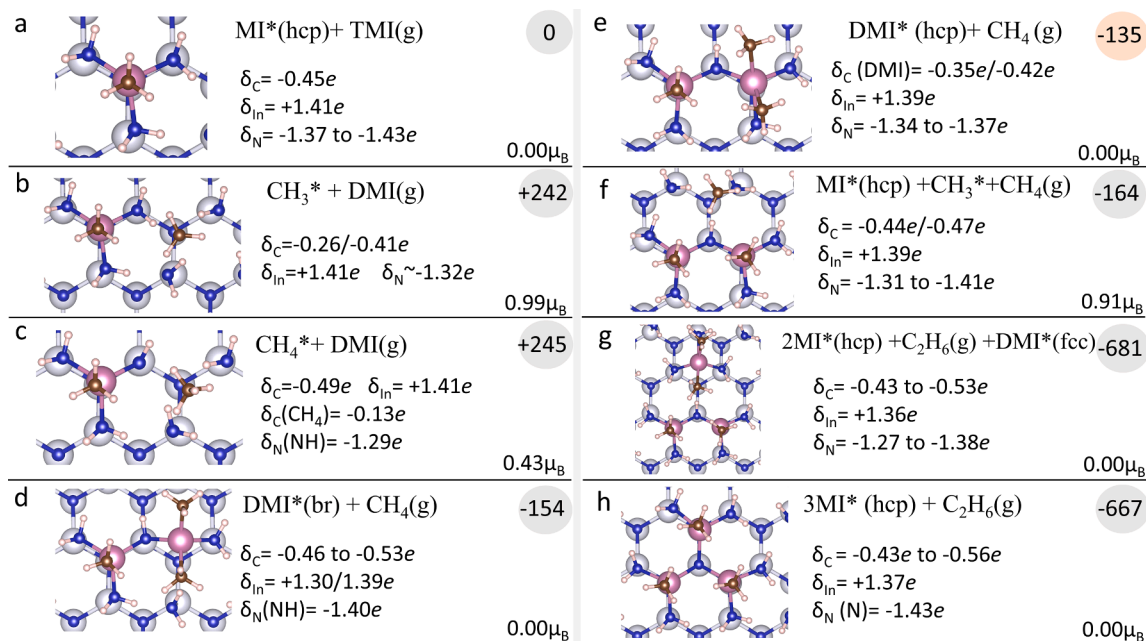
from the TMI and DMI decomposition, leaving CH$_3$ groups at the surface that could form strong C-N bonds with the N-rich layer, instead of the initially presumed In-CH$_3$ bonds in MI*(hcp). Here, the kinetics could also be important to distinguish the CH$_3$ radicals that would effectively be converted in product or be captured by NH or NH$_2$ groups to give rise to impurities. At the end, the downhill approximation from CH$_3$* groups to return C$_2$H$_6$ in an adsorbed configuration leads to E = -508 kJ/mol, whereas the molecular product displays adsorption energy of –21 kJ/mol.

3.3.2 Hydrogen removal from the NH$_2$-terminated surface

During the crystal growth of InN thin film, an important step concerns on the removal of hydrogen atoms from NH$_2$ groups to leave space for the newly In-N bonds that are yet to be formed. Nevertheless, the thermodynamics involved in the decomposition of the first TMI molecule, either in gas phase or on the surface, points out towards a pathway where the initial NH$_2$ groups are left intact upon C$_2$H$_6$ formation. In this subsection, we address this point by considering different routes with H$_2$, C$_2$H$_6$ and/or CH$_4$ production.

Firstly, we have envisioned the H$_2$ formation occurring through the approximation of hydrogen atoms from adjacent NH$_2$ groups that are connected to the MI precursor. The total energy E of +459 kJ/mol found for the final structure, in reference to MI* (hcp), suggests the unfeasibility of this pathway for hydrogen removal. For this reason, we propose a second route involving the addition of a second TMI molecule into the model. This precursor is assumed to follow the decomposition pathways described in subsection 3.3.1, generating DMI and CH$_3$ in gas phase or surface environment. From this point, the decomposition pursues the pathways proposed in Fig. 6 (a-h) and S4 (a-h).

The CH$_3$ adsorption has E= +242 kJ/mol in relation to MI* and TMI (g), which is almost unaltered (<5 kJ/mol) in comparison with the absence of any adsorbate (E= +247 kJ/mol). The H abstraction would then occur with the low barrier of 126 kJ/mol to form CH$_4$, as shown in Fig. 6 (c). The resulting dangling bond at the NH group then leads to an instability that favour the DMI adsorption onto the bridging site. The approximate DMI adsorption energy in presence of the adsorbate is weakened by 29 kJ/mol (E$_{ads}$∼ –377 kJ/mol) in comparison with the

a MI*(hcp)+ TMI(g) — 0
δ$_C$= -0.45e
δ$_{In}$= +1.41e
δ$_N$= -1.37 to -1.43e
0.00μ$_B$

e DMI* (hcp)+ CH$_4$ (g) — -135
δ$_C$ (DMI)= -0.35e/-0.42e
δ$_{In}$= +1.39e
δ$_N$= -1.34 to -1.37e
0.00μ$_B$

b CH$_3$* + DMI(g) — +242
δ$_C$=-0.26/-0.41e
δ$_{In}$=+1.41e δ$_N$~-1.32e
0.99μ$_B$

f MI*(hcp) +CH$_3$*+CH$_4$(g) — -164
δ$_C$= -0.44e/-0.47e
δ$_{In}$= +1.39e
δ$_N$= -1.31 to -1.41e
0.91μ$_B$

c CH$_4$*+ DMI(g) — +245
δ$_C$=-0.49e δ$_{In}$= +1.41e
δ$_C$(CH$_4$)= -0.13e
δ$_N$(NH)= -1.29e
0.43μ$_B$

g 2MI*(hcp) +C$_2$H$_6$(g) +DMI*(fcc) — -681
δ$_C$= -0.43 to -0.53e
δ$_{In}$= +1.36e
δ$_N$= -1.27 to -1.38e
0.00μ$_B$

d DMI*(br) + CH$_4$(g) — -154
δ$_C$= -0.46 to -0.53e
δ$_{In}$= +1.30/1.39e
δ$_N$(NH)= -1.40e
0.00μ$_B$

h 3MI* (hcp) + C$_2$H$_6$(g) — -667
δ$_C$= -0.43e to -0.56e
δ$_{In}$= +1.37e
δ$_N$ (N)= -1.43e
0.00μ$_B$

Fig. 6. Reaction pathways leading to hydrogen removal and MI formation at the hcp position. TMI (g) is first decomposed in gas phase (a) to generate DMI (g) and CH$_3$(g). The latter is physisorbed onto the surface (b), further abstracting a hydrogen atom to yield methane (c). The dangling bond at the NH group is saturated through DMI chemisorption onto the bridge (d) and hcp site (e). In (f-h), it is shown the subsequent DMI chemisorption that releases CH$_3$ radical and leads to the formation of CH$_4$ and ethane molecules in the end of the process.

value obtained on a bare surface (see Table 2). The increased charge transfer to N in NH ($|\Delta\delta| = 0.11e$) confirms the saturation of the chemical bond through the interaction with the DMI precursor in Fig. 6 (d).

The displacement towards the *hcp* site leads to the structure displayed in Fig. 6(e). It is though noticeable that the adsorption onto a presumable stable position is not enough to keep this group attached to the precursor. In fact, one CH_3 group starts to distance itself from the tetrahedral entity, with $d_{In-C} = 2.20$ Å, while reducing its absolute partial charge in comparison with the other CH_3 group ($d_{In-C} = 2.09$ Å, $\delta_C = -0.41e$). The CH_3 release is then a downhill step with $\Delta E = -29$ kJ/mol related to the previous step. From this point, closing the N coordination requires the inclusion of a third DMI molecule into the model after C_2H_6 formation, repeating the aforementioned mechanism towards the MI chemisorption displayed in Fig. 6(h). Alternatively, the mechanism shown in Fig. S4 adds the step concerning the TMI adsorption (b and d). The subsequent adsorption would then require the abstraction of 2H atoms (from nearby NH_2 groups) in order to enable MI formation onto the *hcp* site, resulting in the formation of 2 CH_4 groups as byproducts. This step is not herein described in detail for simplicity reasons.

3.3.3. Trimethylindium decomposition to yield methane

The TMI decomposition leading to CH_4 production is also a possible route to explain the InN crystal growth, similar to the mechanism proposed by An *et al.* for GaN [14]. In this section, we investigate this route from a thermodynamic and kinetic point of view based on the assumptions made in the Section 3.3.1, *i.e.*:

(1) TMI suffers partial decomposition in gas phase to form DMI(g) and CH_3(g).
(2) TMI is stable enough to be physisorbed onto the NH_2-terminated surface.

In case 1, there are still two possibilities to be envisioned depending on the species that first reaches the surface. Although it is unlikely that DMI would be chemisorbed onto the *fcc* or *hcp* site in comparison with the physisorption of the reactive CH_3 radical, such adsorption would lead to C_2H_6, as detailed in the previous section. Thus, we restrain the discussion to the CH_3 adsorption to generate CH_4, as well as the pathway considering that the radical is removed with the flow inside the chamber.

The primary step in this reaction mechanism involves the CH_3 release in gas phase, as discussed in Subsection 3.3.1 (see also Fig. 7 (a) and (b)). Thereafter, the CH_3 physisorption illustrated in Fig. 7 (c) stabilizes the structure in 15 kJ/mol (E= +247 kJ/mol, mag = 0.93 μ_B), in which the radical sits in a near *hcp* position with C···H_2N distance of 2.68–2.88 Å. Naturally, the CH_3 radical exhibits tendency to form a covalent bond with the nitrogen atom from any NH_2 group available on the surface. The interaction strength is confirmed by the stabilization in 344 kJ/mol related to the physisorbed CH_3, as well as by the positive partial charge exhibited by the carbon atom ($\delta_C = +0.25e$, see Fig. 7(d)). Here, it is valid to point out that this structure does not present any magnetization, but it is stable upon application of such effects. In relation to the reference system, *i.e.* TMI (g) and bare surface, the C-N bond formation exhibits E = –97 kJ/mol.

The main obstacles for the adsorbate to reach the step represented in Fig. 7(e), where the first CH_4 molecule is released, correspond to: i) the breakage of the C-N bond at the high cost of 344 kJ/mol and ii) the abstraction of the H atom ($\Delta^{\ddagger}E = +81$ kJ/mol). The unstable NH group has 0.6 μ_B/N atom, thus dimerizing along with the NH_2 group leads to structural stabilization by 195 kJ/mol. On the other hand, it provides another barrier to be overcome before the DMI precursor is adsorbed onto the *hcp* position in Fig. 7 (g). The NH group displays a lower partial charge of $-1.25e$ for the central atom due to the dangling bond, but the shorter distance of 2.14 Å related to the In atom is indicative of a
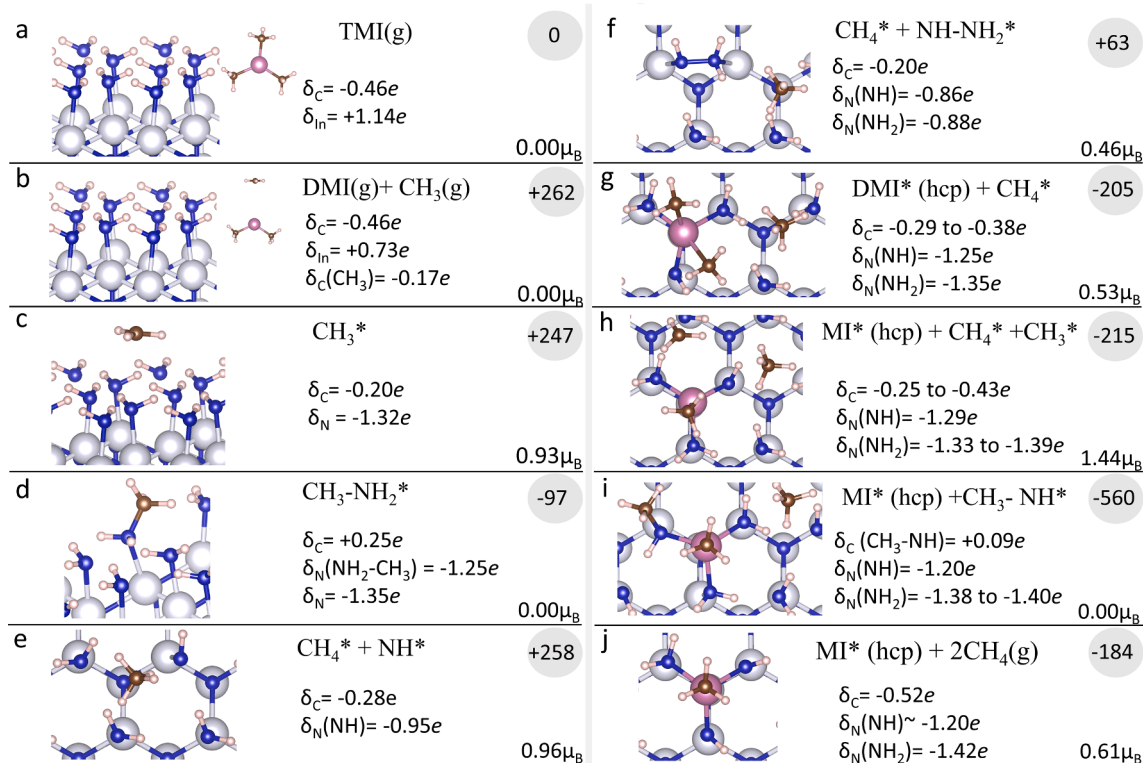
Fig. 7. Reaction pathways for MI and CH_4 formation from TMI decomposition in gas phase, in which 2 NH groups are left on the surface. The initial TMI (g) is first decomposed in gas phase (a-b) to generate DMI(g) and CH_3(g). The latter is physisorbed onto the surface (c), but it forms a C-N chemical bond (d) before abstracting a hydrogen atom to release CH_4 (e). The unstable NH group tends to dimerization (f), which imposes another barrier to be overcome. In (f-i), it is shown the subsequent DMI chemisorption that releases CH_3 radical and leads to CH_4 formation in the end of the process.

stronger chemical bond in comparison with the other interacting NH₂ groups. It is though interesting to notice that, in absolute terms, the partial charge held by the carbon atoms ($\delta_C = -0.29$ to $-0.38e$) is much lower than expected (~-0.5e), a factor that added by the higher distance $d_{In-C} = 2.34$ Å clearly shows that one of the CH₃ groups is not covalently bound to the precursor anymore, but still interacts through dipole–dipole electrostatic forces. Therefore, it is natural that the CH₃ release is a barrierless step with the release of just 10 kJ/mol, which is shown in Fig. 7(h).

From this point, the CH₃ radical is likely to be drawn towards the unstable NH group to form the strong H₃C-NH bond displayed in Fig. 7 (i). For the second hydrogen abstraction that ultimately generates CH₄ in the end of the process, it is first necessary to cleave this chemical bond at the high energy cost of 344 kJ/mol. Hence, this pathway is unlikely to happen from a thermodynamic standpoint, especially when compared with the ethane formation occurring with E = -588 kJ/mol related to TMI(g).

The second route for CH₄ formation as the unique product of TMI decomposition is depicted in Fig. 8 (a-e), in which it is considered that the CH₃ radical is removed with the gas flow inside the chamber. Then DMI could be chemisorbed onto the favourable *fcc* position in a step involving E= -178 kJ/mol. The release of the CH₃ group is barrierless, but the hydrogen abstraction to yield methane requires ~ 106 kJ/mol to occur. The MI precursor is then displaced towards the *hcp* position to generate the final structure at E= –182 kJ/mol. On the other hand, the NH group left in this structure could bond to eventual CH₃ radicals after the next DMI precursor is introduced in the model, a step that would require a high amount of energy to cleave the C-N bond, as discussed before.

### 3.4. The reaction mechanism under ALD experimental conditions

As mentioned in the introductory part, Deminskyi *et al.* [34] carried out the deposition of InN thin film on Si(1 0 0) substrate using atomic layer deposition (ALD) techniques, from TMI and NH₃ plasma as In and N precursors, respectively. The film was deposited in a narrow temperature range (240–260 °C), although a higher crystallinity was found at 320° C (~590 K) alongside self-limiting chemistry [34]. Therefore, these are the conditions of interest in this study, making it important to evaluate the thermal effects over the total energies that are relevant for the reaction- and adsorption- related processes. In this subsection, we explore these effects for the most feasible mechanism, namely the primary C₂H₆ formation upon TMI decomposition, that is followed by the addition of a second molecule for surface hydrogen removal. This

mechanism is still divided into two possibilities depending on whether the TMI decomposition occurs in the surface environment or in gas phase, herein denominated pathways A and B, respectively.

Fig. 9 shows the main steps representing the forenamed pathways, including the relative energies (kJ/mol) for each step to their particular reference system. The results are presented in columns containing the total energies *E,* which are followed by the enthalpy *H*, in boldface blue, and Gibbs free energy *G*, in parenthesis. The activation energies ($\Delta^{\ddagger}X$, where $X = E, H$ or G) are calculated relative to the previous system and depicted in Table 3, for clarity reasons. The analysis is then divided into three parts:

1. **General Aspects.** The structure represented by MI*(hcp) has enthalpy varying in 73 kJ/mol as a result from the choice in reference system, since the TMI adsorption is found to stabilize the structure in the beginning of the process. The steps indicated by A6-A8 and B6-B8 are equivalent, but the following step includes the adsorption of TMI or DMI precursor, respectively. In either case, the final point has H= –630 kJ/mol and G= –647 kJ/mol referenced to MI*(hcp). Furthermore, the steps B1 and B4 differ by the inclusion of the CH₃ physisorption in the latter.

2. **Thermal Effects.** In general, the application of thermal contributions to compose *H* and *G* does not imply in a different qualitative trend. However, including these contributions leads to an averaged variation of 17–29 kJ/mol for these properties, in comparison with E, that is found important for an accurate assessment of the reaction mechanism under the experimental conditions of interest. Here, the pathway A has highest difference in enthalpy (32 kJ/mol) for the last process leading to 3MI*(hcp) formation, whereas this variation reaches 82 kJ/mol for G upon TMI adsorption in A4. Interestingly, the second pathway under consideration is more affected by the application of such effects, changing it up to 49 and 84 kJ/mol for H and G, respectively, after MI*(hcp) formation.

3. **Activation Energies.** In the first route described by A1-A8 steps, the costliest step is the H abstraction represented by A5, with $\Delta^{\ddagger}H = +36$ kJ/mol and $\Delta^{\ddagger}G = +29$ kJ/mol. These values represent a reduction in 26–33 kJ/mol in comparison with the absence of thermal contributions ($\Delta^{\ddagger}E$). In addition, the TMI displacement towards the bridging site also constitutes a relevant step, with $\Delta^{\ddagger}H = +16$ kJ/mol and $\Delta^{\ddagger}G = +28$ kJ/mol.

Moreover, the larger barriers imposed by the decomposition in gas phase constitute a trend that is, unsurprisingly, unaffected upon calculation of $\Delta^{\ddagger}H$ and $\Delta^{\ddagger}G$. Table 3 shows that the steps concerning the TMI
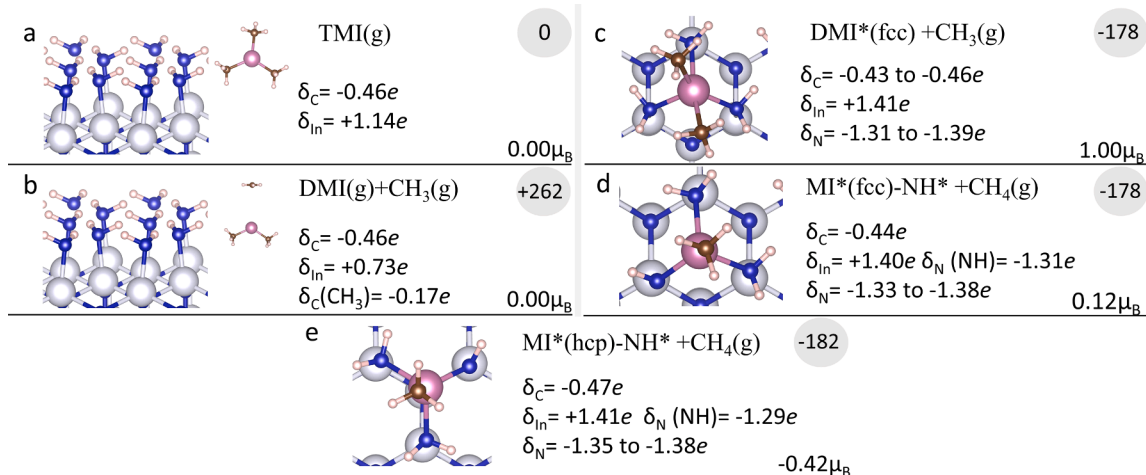
Fig. 8. Reaction pathways for MI and CH₄ formation from TMI decomposition in gas phase, in which 1 NH group is left on the surface. The initial TMI (g) is first decomposed in gas phase (a-b) to generate DMI(g) and CH₃(g). The former is chemisorbed onto the *fcc* position at the surface (c), further releasing CH₄ and leaving MI in the same position (d). The low barrier to reach the *hcp* site enables the displacement to generate the final structure in (e).
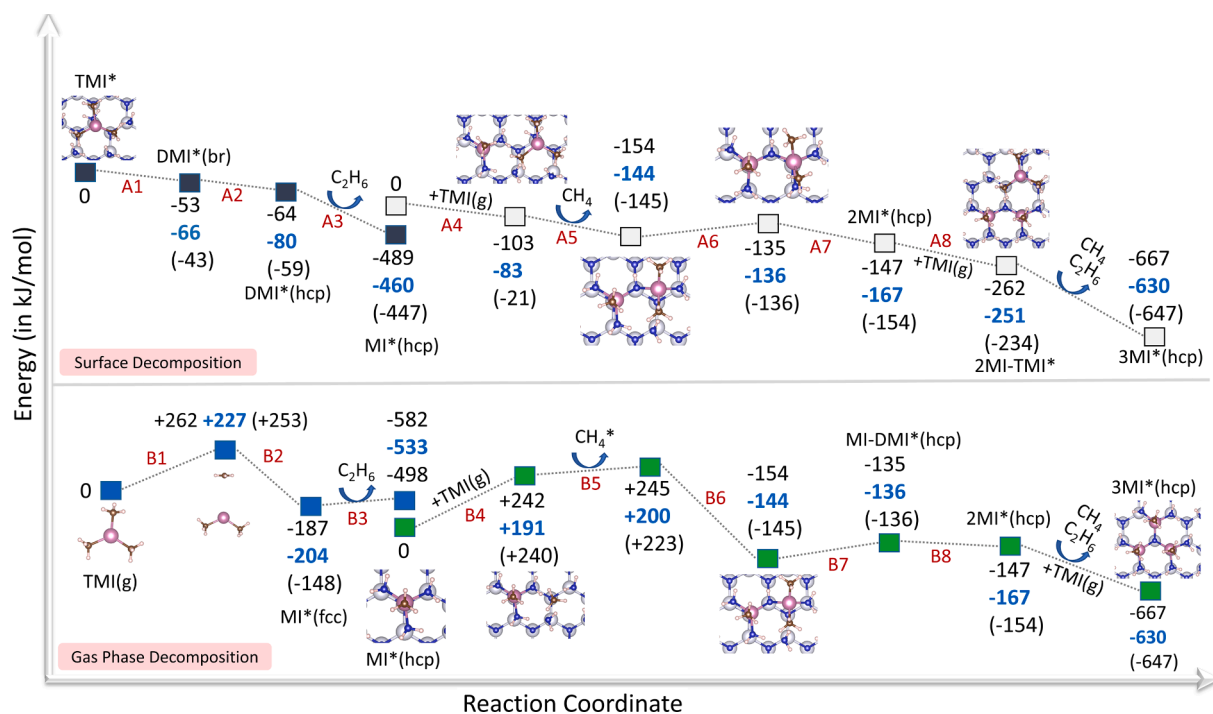
Fig. 9. Reaction pathways for the most plausible routes for TMI decomposition leading to the InN crystal growth at T = 0 K and under ALD experimental conditions (T = 590 K). The relative energies at 0 K (E), enthalpy (H) and Gibbs free energy (G) are, respectively, given by the values in black, boldface blue and in parenthesis. The asterisk (*) indicates an adsorbed species. Note that the reference system is changed at the point given by MI*(hcp). DMI* (hcp) and MI-DMI*(hcp) are minimum points in the PES under non-spin polarization conditions, but the CH_3 release is barrierless upon application of such effects.

Table 3

Activation barriers (in kJ/mol) for the main processes related to the TMI decomposition into MI at T = 0 and 590 K. The dashed lines represent barrierless steps. Level of theory: 425 eV/1–1–1 k-points.

	$\Delta^{\ddagger}E(0\ K)$	$\Delta^{\ddagger}H(590\ K)$	$\Delta^{\ddagger}G(590\ K)$
Surface Decomposition			
A1	+22	+16	+28
A2	+21	+11	+12
A3	–	–	–
A4	–	–	–
A5	+62	+36	+29
A6	+19	+9	+10
A7	–	–	–
A8	–	–	–
Gas Phase Decomposition			
B1	+262	+227	+253
B2	–	–	–
B3	+14	+16	+3
B4	+242	+191	+240
B5	+125	+103	+125
B6	–	–	–
B7	+19	+9	+10
B8	–	–	–

decomposition in gas phase are the costliest, with $\Delta^{\ddagger}H$ = +191–227 kJ/mol and $\Delta^{\ddagger}G$ = +240–253 kJ/mol, representing a variation of up to + 51 kJ/mol for $\Delta^{\ddagger}H$ related to $\Delta^{\ddagger}E$.

Hence, the mechanism A is the most plausible from a thermodynamic and kinetic standpoint under the experimental conditions for thin film deposition. Here, the role of the gas phase decomposition of the TMI precursor should clarify the feasibility of the second pathway, which is an ongoing work that will be presented as a future publication.

4. Conclusions

In this contribution, we investigated different reaction pathways leading to the InN crystal growth using atomic scale modelling. The wurtzite InN has chemical bonds with predominant covalent character, and bulk properties that are in fair agreement with the literature reports.

The (1x1) slab model has calculated surface energy γ = 1.91 J/m^2 at the 775 eV/9–9–1 k-points level of theory. In this system, the saturation of the dangling bond at the bottommost layer stabilizes the crystal structure and eliminates the magnetization that is inherently arising from N atoms. The reconstruction process is well reproduced through the (2x1) surface expansion, where the alternation between trigonal planar and tetrahedral *In* atoms leads to an approximate unpaired electron on the latter.

The N-rich layer is characterized by the NH_2-terminated surface resulting from NH_3 decomposition. In this sense, each NH_2 group should form a covalent or coordinate covalent bond while sitting on the *top* position, depending on whether the interaction occurs with the tetrahedral or trigonal planar In atom. Thus, the full coverage by NH_2 radicals leaves between 1 and 2 electrons available for building the In-rich layer, as the remaining lone pair from NH_2 radical should be equally distributed among the other groups. Moreover, the passivation method by either regular or fractionally charged H atoms does not affect the thermodynamic properties that were studied in this work.

In the next step, the (3x2) slab model was used for modelling the TMI decomposition in gas phase or in the surface environment. In the latter case, TMI is preferentially physisorbed onto the *top* position, with E_{ads} = –92 kJ/ mol. The first CH_3 elimination occurs with release of 75 kJ/mol, but the In precursor should first overcome the small barrier of $\Delta^{\ddagger}E/\Delta^{\ddagger}H$ = +22/16 kJ/mol to reach the bridging site. The further DMI displacement towards the *hcp* site involves a similar activation barrier, leading to the second CH_3 release and C_2H_6 formation in gas phase. This pathway requires the second/third TMI adsorption nearby the MI adsorbate for hydrogen removal from the NH_2-terminated surface. The costliest step is found associated to CH_4 production ($\Delta^{\ddagger}E/\Delta^{\ddagger}H$ = +62/36 kJ/mol). Alternatively, the physisorbed CH_3 groups could form a strong covalent bond with the NH_2 group from the N-rich layer, which not only confirms the radical nature of the chemisorbed NH_2 group, but also

imposes a large barrier for its release in the upcoming reactions. In this case, this step would not contribute to the In-rich layer formation.

Declaration of Competing Interest

The authors declare that they have no known competing financial interests or personal relationships that could have appeared to influence the work reported in this paper.

Acknowledgements

Appendix A. Supplementary material

Supplementary data to this article can be found online at https://doi.org/10.1016/j.apsusc.2022.153290.

References

[1] M.H. Chang, D. Das, P.V. Varde, M. Pecht, Light emitting diodes reliability review, Microelectron. Reliab. 52 (5) (2012) 762–782, https://doi.org/10.1016/j.microrel.2011.07.063.

[2] T. Guner, M.M. Demir, A Review on Halide Perovskites as Color Conversion Layers in White Light Emitting Diode Applications, Phys. Status Solidi Appl. Mater. Sci. 215 (13) (2018) 1800120, https://doi.org/10.1002/pssa.201800120.

[3] M. Manikandan, D. Nirmal, J. Ajayan, P. Mohankumar, P. Prajoon, L. Arivazhagan, A review of blue light emitting diodes for future solid state lighting and visible light communication applications, Superlattices Microstruct. 136 (2019) 106294, https://doi.org/10.1016/j.spmi.2019.106294.

[4] M. Loi, A. Villani, F. Paciolla, G. Mulè, C. Paciolla, Challenges and opportunities of light-emitting diode (Led) as key to modulate antioxidant compounds in plants. a review, Antioxidants. 10 (1) (2021) 42, https://doi.org/10.3390/antiox10010042.

[5] D.R. Opel, E. Hagstrom, A.K. Pace, K. Sisto, S.A. Hirano-Ali, S. Desai, J. Swan, Light-emitting diodes: A brief review and clinical experience 6th, 8, J. Clin. Aesthet Dermatol, 2015, pp. 36–44.

[6] K.V.R.M. Murali, V.B. Naik, D. Datta, Gallium-nitride-based light-emitting diodes: 2014 Nobel Prize in Physics, Resonance 20 (2015) 605–615, https://doi.org/10.1007/s12045-015-0219-y.

[7] J. Amano, H.;Sawaki,N.; Akasaki, Metalorganic Vapor Phase Epitaxial Growth of A high quality GaN film using an AlIn buffer layer, Appl. Phys. Lett. 48 (1986) 353–355.

[8] S. Nakamura, Related content GaN Growth Using GaN Buffer Layer, Jpn. J. Appl. Phys. 30 (Part 2, No. 10A) (1991) L1705–L1707.

[9] A. Belabbes, L.C. De Carvalho, A. Schleife, F. Bechstedt, Cubic inclusions in hexagonal AlN, GaN, and InN: Electronic states, Phys. Rev. B - Condens. Matter Mater. Phys. 84 (2011) 125108, https://doi.org/10.1103/PhysRevB.84.125108.

[10] N. Kuwano, T. Shiraishi, A. Koga, K. Oki, K. Hiramatsu, H. Amano, K. Itoh, I. Akasaki, Cross-sectional TEM study of microstructures in MOVPE GaN films grown on α-Al2O3 with a buffer layer of AlN, J. Cryst. Growth. 115 (1-4) (1991) 381–387, https://doi.org/10.1016/0022-0248(91)90772-W.

[11] S. Nakamura, T. Mukai, M. Senoh, High-Power GaN P-N Junction Blue-Light-Emitting Diodes, Jpn. J. Appl. Phys. 30 (Part 2, No. 12A) (1991) L1998–L2001.

[12] S.P. Denbaars, D. Feezell, K. Kelchner, S. Pimputkar, C.C. Pan, C.C. Yen, S. Tanaka, Y. Zhao, N. Pfaff, R. Farrell, M. Iza, S. Keller, U. Mishra, J.S. Speck, S. Nakamura, Development of gallium-nitride-based light-emitting diodes (LEDs) and laser diodes for energy-efficient lighting and displays, Acta Mater. 61 (3) (2013) 945–951, https://doi.org/10.1016/j.actamat.2012.10.042.

[13] B. Amiri, A. Lazreg, F.A. Bensaber, Optical and Thermoelectric properties of Gd doped Wurtzite GaN, Optik 2021 (240) (2021) 166798, https://doi.org/10.1016/j.ijleo.2021.166798.

[14] Q. An, A. Jaramillo-Botero, W.G. Liu, W.A. Goddard, Reaction pathways of GaN (0001) growth from trimethylgallium and ammonia versus triethylgallium and hydrazine using first principle calculations, J. Phys. Chem. C. 119 (8) (2015) 4095–4103, https://doi.org/10.1021/jp5116405.

[15] C.C. Liu, Y.H. Chen, M.P. Houng, Y.H. Wang, Y.K. Su, W. Bin Chen, S.M. Chen, Improved light-output power of GaN LEDs by selective region activation, IEEE Photonics Technol. Lett. 16 (6) (2004) 1444–1446, https://doi.org/10.1109/LPT.2004.826786.

[16] D. Xu, H. Yang, J.B. Li, S.F. Li, Y.T. Wang, D.G. Zhao, R.H. Wu, Initial stages of GaN/GaAs (100) growth by metalorganic chemical vapor deposition, J. Electron. Mater. 29 (2) (2000) 177–182, https://doi.org/10.1007/s11664-000-0138-9.

[17] P. Rouf, R. Samii, K. Rönnby, B. Bakhit, S.C. Buttera, I. Martinovic, L. Ojamäe, C. W. Hsu, J. Palisaitis, V. Kessler, H. Pedersen, N.J. O'Brien, Hexacoordinated Gallium(III) Triazenide Precursor for Epitaxial Gallium Nitride by Atomic Layer Deposition, Chem. Mater. 33 (9) (2021) 3266–3275, https://doi.org/10.1021/acs.chemmater.1c00244.

[18] V. Kumaresan, L. Largeau, A. Madouri, F. Glas, H. Zhang, F. Oehler, A. Cavanna, A. Babichev, L. Travers, N. Gogneau, M. Tchernycheva, J.C. Harmand, Epitaxy of GaN Nanowires on Graphene, Nano Lett. 16 (8) (2016) 4895–4902, https://doi.org/10.1021/acs.nanolett.6b01453.

[19] Y. Yu, T. Wang, X. Chen, L. Zhang, Y. Wang, Y. Niu, J. Yu, H. Ma, X. Li, F. Liu, G. Deng, Z. Shi, B. Zhang, X. Wang, Y. Zhang, Demonstration of epitaxial growth of strain-relaxed GaN films on graphene/SiC substrates for long wavelength light-emitting diodes, Light Sci. Appl. 10 (2021) 117, https://doi.org/10.1038/s41377-021-00560-3.

[20] Y. Zhang, Z. Chen, K. Zhang, Z. Feng, H. Zhao, Laser-Assisted Metal-Organic Chemical Vapor Deposition of Gallium Nitride, Phys. Status Solidi - Rapid Res. Lett. 15 (6) (2021) 2100202, https://doi.org/10.1002/pssr.202100202.

[21] I. Akasaki, H. Amano, S. Sota, H. Sakai, T. Tanaka, MasayoshiKoike, Stimulated Emission by Current Injection from an AlGaN/GaN/GaInN Quantum Well Device, Jpn. J. Appl. Phys. 34 (Part 2) (11B) (1995) L1517–L1519, https://doi.org/10.1143/jjap.34.l1517.

[22] S. Nakamura, M. Senoh, Nagahama, N. Iwasa, T. Yamada, T. Matsushita, H. Kiyoku, Y. Sugimoto, InGaN-based multi-quantum-well-structure laser diodes, Jpn. J. Appl. Phys. 35 (1996) L74, https://doi.org/10.1143/jjap.35.l74.

[23] S. Nakamura, The roles of structural imperfections in InGaN-based blue light-emitting diodes and laser diodes, Science 281 (5379) (1998) 956–961, https://doi.org/10.1126/science.281.5379.956.

[24] D.S. Arteev, A.V. Sakharov, A.E. Nikolaev, W.V. Lundin, A.F. Tsatsulnikov, Temperature-dependent luminescent properties of dual-wavelength InGaN LEDs, J. Lumin. 234 (2021) 117957, https://doi.org/10.1016/j.jlumin.2021.117957.

[25] J. Wu, When group-III nitrides go infrared: New properties and perspectives, J. Appl. Phys. 106 (2009) 011101, https://doi.org/10.1063/1.3155798.

[26] C.H. Chen, S.J. Chang, Y.K. Su, G.C. Chi, J.K. Sheu, J.F. Chen, High-efficiency InGaN-GaN MQW green light-emitting diodes with CART and DBR structures, IEEE J. Sel. Top. Quantum Electron. 8 (2) (2002) 284–288, https://doi.org/10.1109/2944.999182.

[27] O. Jani, C. Honsberg, Y. Huang, J.O. Song, I. Ferguson, G. Namkoong, E. Trybus, A. Doolittle, S. Kurtz, Design, growth, fabrication and characterization of high-band GAP InGaN/GaN solar cells, in: Conf. Rec. 2006 IEEE 4th World Conf. Photovolt. Energy Conversion, WCPEC-4, 2006. 10.1109/WCPEC.2006.279337.

[28] B.H. Cardelino, C.A. Cardelino, Adsorption and dissociation of trimethylindium on an indium nitride substrate. A computational study, J. Phys. Chem. C. 113 (52) (2009) 21765–21778, https://doi.org/10.1021/jp907426r.

[29] A.G. Bhuiyan, A. Hashimoto, A. Yamamoto, Indium nitride (InN): A review on growth, characterization, and properties, J. Appl. Phys. 94 (2003) 2779, https://doi.org/10.1063/1.1595135.

[30] B.A. Andreev, K.E. Kudryavtsev, A.N. Yablonskiy, D.N. Lobanov, P.A. Bushuykin, L. V. Krasilnikova, E.V. Skorokhodov, P.A. Yunin, A.V. Novikov, V.Y. Davydov, Z. F. Krasilnik, Towards the indium nitride laser: Obtaining infrared stimulated emission from planar monocrystalline InN structures, Sci. Rep. 8 (2018) 9454, https://doi.org/10.1038/s41598-018-27911-2.

[31] R. Togashi, T. Kamoshita, Y. Nishizawa, H. Murakami, Y. Kumagai, A. Koukitu, Experimental and ab-initio studies of temperature dependent InN decomposition in various ambient, Phys. Status Solidi Curr. Top. Solid State Phys. 5 (6) (2008) 1518–1521, https://doi.org/10.1002/pssc.200778434.

[32] M. Kučera, A. Adikimenakis, E. Dobročka, R. Kúdela, M. Ťapajna, A. Laurenčíková, A. Georgakilas, J. Kuzmík, Structural, electrical, and optical properties of annealed InN films grown on sapphire and silicon substrates, Thin Solid Films 672 (2019) 114–119, https://doi.org/10.1016/j.tsf.2019.01.006.

[33] S. Ruffenach, M. Moret, O. Briot, B. Gil, Recent advances in the MOVPE growth of indium nitride, Phys. Status Solidi Appl. Mater. Sci. 207 (1) (2010) 9–18, https://doi.org/10.1002/pssa.200982642.

[34] P. Deminskyi, P. Rouf, I.G. Ivanov, H. Pedersen, Atomic layer deposition of InN using trimethylindium and ammonia plasma, J. Vac. Sci. Technol. A. 37 (2019) 020926, https://doi.org/10.1116/1.5079279.

[35] N.J. O'Brien, P. Rouf, R. Samii, K. Rönnby, S.C. Buttera, C.W. Hsu, I.G. Ivanov, V. Kessler, L. Ojamäe, H. Pedersen, In Situ Activation of an Indium(III) Triazenide Precursor for Epitaxial Growth of Indium Nitride by Atomic Layer Deposition, Chem. Mater. 32 (11) (2020) 4481–4489, https://doi.org/10.1021/acs.chemmater.9b05171.

[36] H. Pedersen, S.D. Elliott, Studying chemical vapor deposition processes with theoretical chemistry, Theor. Chem. Acc. 133 (2014) 1–10, https://doi.org/10.1007/s00214-014-1476-7.

[37] N.E. Richey, C. De Paula, S.F. Bent, Understanding chemical and physical mechanisms in atomic layer deposition, J. Chem. Phys. 152 (2020) 040902, https://doi.org/10.1063/1.5133390.

[38] W. Walkosz, P. Zapol, G.B. Stephenson, A DFT study of reaction pathways of NH$_3$ decomposition on InN (0001) surface, J. Chem. Phys. 137 (2012) 054708, https://doi.org/10.1063/1.4739309.

[39] K. Rönnby, H. Pedersen, L. Ojamäe, Surface structures from NH$_3$ chemisorption in CVD and ALD of AlN , GaN and InN films, J. Phys. Chem. C (2022), https://doi.org/10.1021/acs.jpcc.2c00510.

[40] N. Cheimarios, G. Kokkoris, A.G. Boudouvis, Multiscale Modeling in Chemical Vapor Deposition Processes: Models and Methodologies, Arch. Comput. Methods Eng. 28 (2021) 637–672, https://doi.org/10.1007/s11831-019-09398-w.

[41] J.Y. Hwang, C. Park, J.H. Jung, T.J. Anderson, Homogeneous Decomposition of Trimethylindium in an Inverted, Stagnation-Point Flow Reactor by In Situ Raman Spectroscopy, J. Electrochem. Soc. 155 (2008) H124, https://doi.org/10.1149/1.2816206.

[42] G. Kresse, J. Furthmüller, Software VASP, Phys. Rev. B, Vienna, 1996.

[43] J.P. Perdew, K. Burke, M. Ernzerhof, Generalized gradient approximation made simple, Phys. Rev. Lett. 77 (18) (1996) 3865–3868, https://doi.org/10.1103/PhysRevLett.77.3865.

[44] S. Grimme, J. Antony, S. Ehrlich, H. Krieg, A consistent and accurate ab initio parametrization of density functional dispersion correction (DFT-D) for the 94 elements H-Pu, J. Chem. Phys. 132 (2010) 154104, https://doi.org/10.1063/1.3382344.

[45] R.W.G. Wyckoff, Crystal Structures John Wiley, New York (1963).

[46] W. Sun, G. Ceder, Efficient creation and convergence of surface slabs, Surf. Sci. 617 (2013) 53–59, https://doi.org/10.1016/j.susc.2013.05.016.

[47] A. Togo, I. Tanaka, First principles phonon calculations in materials science, Scr. Mater. 108 (2015) 1–5, https://doi.org/10.1016/j.scriptamat.2015.07.021.

[48] G. Henkelman, B.P. Uberuaga, H. Jónsson, Climbing image nudged elastic band method for finding saddle points and minimum energy paths, J. Chem. Phys. 113 (2000) 9901, https://doi.org/10.1063/1.1329672.

[49] H. Jónsson, G. Mills, K.W. Jacobsen, Nudged elastic band method for finding minimum energy paths of transitions, in Classical and Quantum Dynamics in Condensed Phase Simulations (1998) 385–404, https://doi.org/10.1142/9789812839664_0016.

[50] D. Sheppard, P. Xiao, W. Chemelewski, D.D. Johnson, G. Henkelman, A generalized solid-state nudged elastic band method, J. Chem. Phys. 136 (2012) 074103, https://doi.org/10.1063/1.3684549.

[51] J. Nord, K. Albe, P. Erhart, K. Nordlund, Modelling of compound semiconductors: Analytical bond-order potential for gallium, nitrogen and gallium nitride, J. Phys. Condens. Matter. 15 (2003) 5649–5662, https://doi.org/10.1088/0953-8984/15/32/324.

[52] H. Neumann, J. H. Edgar (ed.). Properties of Group III Nitrides. (EMIS Datareviews Series No. 11). INSPEC, The Institution of Electrical Engineers, London 1994. 302 Seiten, 121 Abbildungen, 77 Tabellen. ISBN 0–85296–818–3, Cryst. Res. Technol. (1995). 10.1002/crat.2170300704.

[53] A. Zoroddu, F. Bernardini, P. Ruggerone, V. Fiorentini, First-principles prediction of structure, energetics, formation enthalpy, elastic constants, polarization, and piezoelectric constants of AlN, GaN, and InN: Comparison of local and gradient-corrected density-functional theory, Phys. Rev. B - Condens. Matter Mater. Phys. 64 (2001) 045208, https://doi.org/10.1103/PhysRevB.64.045208.

[54] I. Gorczyca, J. Plesiewicz, L. Dmowski, T. Suski, N.E. Christensen, A. Svane, C. S. Gallinat, G. Koblmueller, J.S. Speck, Electronic structure and effective masses of InN under pressure, J. Appl. Phys. 104 (2008) 013704, https://doi.org/10.1063/1.2953094.

[55] O.K. Semchinova, J. Aderhold, J. Graul, A. Filimonov, H. Neff, Photoluminescence, depth profile, and lattice instability of hexagonal InN films, Appl. Phys. Lett. 94 (2003) 4457, https://doi.org/10.1063/1.1634691.

[56] J. Wu, W. Walukiewicz, W. Shan, K.M. Yu, J.W. Ager, S.X. Li, E.E. Haller, H. Lu, W. J. Schaff, Temperature dependence of the fundamental band gap of InN, J. Appl. Phys. 94 (4457) (2003), https://doi.org/10.1063/1.1605815.

[57] B. Arnaudov, I. Akasaki, P.P. Paskov, B. Magnusson, E. Valcheva, B. Monemar, H. Lu, W.J. Schaff, H. Amano, Energy position of near-band-edge emission spectra of InN epitaxial layers with different doping levels, Phys. Rev. B - Condens. Matter Mater. Phys. 69 (2004) 115216, https://doi.org/10.1103/PhysRevB.69.115216.

[58] D. Liang, R. Quhe, Y. Chen, L. Wu, Q. Wang, P. Guan, S. Wang, P. Lu, Electronic and excitonic properties of two-dimensional and bulk InN crystals, RSC Adv. 7 (2017) 42455–42461, https://doi.org/10.1039/c7ra07640a.

[59] G. Guisbiers, D. Liu, Q. Jiang, L. Buchaillot, Theoretical predictions of wurtzite III-nitride nano-materials properties, Phys. Chem. Chem. Phys. 12 (2010) 7203–7210, https://doi.org/10.1039/c002496a.

[60] P. Mori-Sánchez, A.J. Cohen, W. Yang, Localization and delocalization errors in density functional theory and implications for band-gap prediction, Phys. Rev. Lett. 100 (2008) 146401, https://doi.org/10.1103/PhysRevLett.100.146401.

[61] G.B. Damas, L.T. Costa, R. Ahuja, C.M. Araujo, Understanding carbon dioxide capture on metal-organic frameworks from first-principles theory: The case of MIL-53(X), with X = Fe3+, Al3+, and Cu2+, J. Chem. Phys. 155 (2021) 024701, https://doi.org/10.1063/5.0054874.

[62] M.F.J. Vos, G. Van Straaten, W.M.M.E. Kessels, A.J.M. Mackus, Atomic Layer Deposition of Cobalt Using H2-, N2-, and NH3-Based Plasmas: On the Role of the Co-reactant, J. Phys. Chem. C. 122 (39) (2018) 22519–22529, https://doi.org/10.1021/acs.jpcc.8b06342.

[63] A. Pakkala, M. Putkonen, Atomic Layer Deposition, Handb. Depos. Technol. Film. Coatings (2010), https://doi.org/10.1016/B978-0-8155-2031-3.00008-9.

[64] D.R. Lide, Electronegativity in CRC Handbook of Chemistry and Physics, CRC Press, Boca Raton, FL, 2005.

[65] B.H. Cardelino, C.E. Moore, C.A. Cardelino, D.O. Frazier, K.J. Bachmann, Theoretical study of indium compounds of interest for organometallic chemical vapor deposition, J. Phys. Chem. A. 105 (5) (2001) 849–868, https://doi.org/10.1021/jp0013558.

[66] C.K. Ande, H.C.M. Knoops, K. de Peuter, M. van Drunen, S.D. Elliott, W.M. M. Kessels, Role of Surface Termination in Atomic Layer Deposition of Silicon Nitride, J. Phys. Chem. Lett. 6 (18) (2015) 3610–3614, https://doi.org/10.1021/acs.jpclett.5b01596.

[67] P. Rouf, N.J. O'Brien, K. Rönnby, R. Samii, I.G. Ivanov, L. Ojamäe, H. Pedersen, The Endocyclic Carbon Substituent of Guanidinate and Amidinate Precursors Controlling Atomic Layer Deposition of InN Films, J. Phys. Chem. C. 123 (42) (2019) 25691–25700, https://doi.org/10.1021/acs.jpcc.9b07005.

[68] A. Haider, S. Kizir, N. Biyikli, Low-temperature self-limiting atomic layer deposition of wurtzite InN on Si(100), AIP Adv. 6 (2016) 045203, https://doi.org/10.1063/1.4946786.